International Journal of Heat and Mass Transfer 102 (2016) 1100–1107

Contents lists available at ScienceDirect

International Journal of Heat and Mass Transfer

journal homepage: www.elsevier.com/locate/ijhmt

Surface roughening for hemi-wicking and its impact on convective boiling heat transfer

Beom Seok Kim [a,1], Geehong Choi [b,1], Dong Il Shim [b], Kyung Min Kim [b], Hyung Hee Cho [b,*]

[a] IFW Dresden, P. O. Box 270116, 01171 Dresden, Germany
[b] Department of Mechanical Engineering, Yonsei University, 03722 Seoul, Republic of Korea

ARTICLE INFO

Article history:
Received 6 August 2015
Received in revised form 13 January 2016
Accepted 2 July 2016
Available online 19 July 2016

Keywords:
Hemi-wicking
Surface wetting
Surface roughness
Boiling heat transfer
Convective heat transfer

ABSTRACT

Superhydrophilicity accompanying hemi-wicking driven by interfacial capillary force can be induced by constructing interfacial structures. We uncover the underlying mechanism for the morphologically driven hemi-wicking, and extend its impact into the practical heat transferring scheme of convective boiling system: the morphologically-driven hemi-wicking on a roughened interface can contribute greatly to the enhancement of boiling heat transfer performance of the convective heat dissipation capacity of critical heat flux (CHF). We present design prerequisites on controlling characteristic lengths of nanoscale interfacial structures that initiate hemi-wicking and consequently enhance boiling performance. Interfacial liquid refreshing through morphologically driven hemi-wicking leads to a greater than 100% increase in CHF by roughening surfaces using vertically aligned silicon nanowire structures (SiNWs). We confirm strong wicking characteristics are essential to increase CHF, however it must be differentiated from surface roughening. Even though the roughening is a prerequisite for leading to the wicking, it can even deteriorate CHF without involving advantage of the interfacial re-wetting. Dimensional prerequisites that initiate hemi-wicking by modulating the characteristic length of SiNWs can be design guidelines for pragmatic engineering applications to enhance feasibility and reliability. We use our findings to put forward a guideline to improve boiling performance, and suggest a way to make breakthrough in heat and energy transfer systems through the functionalized interface.

1. Introduction

Interfacial morphology is a principal determinant of the wetting characteristics of an interface. Based on Young's equation describing the behavior of liquids on a solid surface in equilibrium, wetting can be considered a physical function of geometric variables regarding morphology [1–5]. In particular, superhydrophilicity accompanying hemi-wicking driven by interfacial capillary force can be induced by constructing interfacial structures under a specific design criterion [6–9]. The criterion for hemi-wicking can be expressed as [10,11]:

$$\theta_c > \theta^*, \quad \cos\theta_c = (1-\varphi)/(r-\varphi), \tag{1}$$

where θ_c, θ^*, φ, and r are the critical contact angle (CA) demanded as a prerequisite, equilibrium CA on an ideal surface, solid fraction of the solid–liquid interface contacting the liquid droplet, and roughness factor defined as the ratio of an actual to projected surface area, respectively. This equation allows us to design a functional interface by roughening and manipulating characteristic lengths of the interfacial structures.

One highly promising applications of superhydrophilicity with hemi-wicking is boiling heat transfer, which is a powerful method for dissipating and transferring thermal energy [12–15]. In convective boiling heat transfer, nucleation and convective behavior of the two-phase mixture of coolant and bubbles are determined by the characteristics of the interface [16–19]. In particular, liquid refreshing against the dry-out of a boiling surface is obviously dependent on the roughness and wetting characteristics of the interface [20,21]. This is due to interfacial hydrodynamics dominating the nucleation of bubbles, liquid supply/refreshing toward nucleation sites against upward bubble detachment, and convective mixing of the multiphase flow. Recent studies have attempted to enhance principal boiling performance of the maximum heat dissipation capacity (i.e., critical heat flux, CHF) allowed without any irreversible thermal failure of a system, and the convective dissipation efficiency (i.e., heat transfer coefficient, HTC) for effective thermal energy dissipation by promoting interfacial functionalities using micro/nano- and hierarchical structures [13,22–26]. They

* Corresponding author. Fax: +82 2 312 2159.
E-mail address: hhcho@yonsei.ac.kr (H.H. Cho).
[1] These authors contributed equally to this work.

http://dx.doi.org/10.1016/j.ijheatmasstransfer.2016.07.008
0017-9310/

reported that the roughened surfaces and their by-productive strong wicking ability could be favorable to succeed in improving boiling performance. By adopting feasible approaches for strong refreshing via hemi-wicking, CHF could be improved by more than 100% [26,27]. Roughening of interfaces has been proved favorable to initiate nucleation readily and effective to induce hemi-wicking.

While inducing hemi-wicking through morphological manipulations, we demonstrate that convective boiling heat transfer can be controlled by modulating the surface roughness factor and consequential wetting characteristics. We demonstrate that hydrodynamic hemi-wicking on an interface can govern the maximum heat dissipation capacity of CHF. The morphological roughening via nanostructures and its impact on interfacial hydrodynamic effects accompanying hemi-wicking for liquid assessment towards boiling surface can be favorable for the extension of CHF. We suggest that the morphologically-induced wicking effects for liquid assessment must be distinguished from an analogous liquid spreading which can be alternatively obtained from a low-surface tension liquid like a typical refrigerant of FC-72. Interfacial liquid refreshing through morphologically driven hemi-wicking is realized by roughening surfaces using vertically aligned silicon nanowire structures (SiNWs). Dimensional prerequisites initiating hemi-wicking are theoretically discussed with regard to the characteristic length of SiNWs' height, which should be controlled for feasible applications. Using two different kinds of working fluids, deionized (DI) water and a refrigerant (FC-72), we differentiate the hydrodynamic characteristics of wicking from the static wetting characteristics, which simply show low apparent CAs. The peculiarity of interfacial characteristics is evaluated under a forced convective boiling for a possible application to pragmatic and feasible heat dissipating cooling systems. It is verified that morphologically-driven hemi-wicking is essential to promote CHF in convective boiling heat transfer, and convective dissipation efficiency regarding HTC is enhanced by nucleation-favorable surfaces with a highly roughened morphology.

2. Materials and methods

2.1. Heat transfer sensor with in-situ SiNWs

A sensor to evaluate heat transfer is designed with arrays of resistance temperature detectors (RTDs), a thin film heater, and nanowires which are synthesized *in situ* on the bare surface of the sensor (as shown in Fig. 1(a–c)). The sensor is fabricated on a p-type silicon substrate (boron-doped, (100) orientation, resistivity of 1–10 Ω·cm) with the thickness of 500 μm. First, the Si substrate is cleaned in a piranha solution (3:1 mixture of H_2SO_4 and H_2O_2 by volume) for more than 40 min. Then the substrate is further cleaned with acetone and methanol for 5 min each in turn using a sonicator. After the substrate cleaning, UV lithography and platinum (Pt) deposition using an e-beam evaporator are conducted for the lift-off of the Pt layer. Pt patterns with a serpentine shape are used as RTDs by linearly varying the resistance according to temperature. An insulating oxide-nitride-oxide multilayer is then deposited on the RTDs. After additional lithography and reactive ion etching for the selective removal of the insulating layer from the RTD electrodes, we deposit an 800-nm-thick indium tin oxide (ITO) layer with sequential etching of the ITO for heater formation. Gold electrodes are formed on both tips of the heater by Au lift-off. The sensor has five sets of four-wire RTDs and a thin film heater with an area of $0.5 \times 1.0\ cm^2$. The top-down nanowires are synthesized on the opposite side of the Si substrate after the completion of the sensor fabrication. Before the boiling experiment, we calibrate the sensor to determine the correlation between temperature and resistance of each RTD. We translate the resistances from local RTDs into temperatures through four-wire circuits, and determine the linear variation within experimental temperature ranges. For most of the fabricated RTDs, a 1.5 Ω difference is approximately seen with a one degree centigrade change in temperature [25,26]. In this study, boiling performance is evaluated using local temperature measurements from RTD located in the center of the heating area.

2.2. Synthesis of SiNWs using a metal-assisted chemical etching method [28]

Metal-assisted chemical etching (MaCE) is employed to synthesize vertically aligned SiNWs on a Si substrate of the fabricated sensor [25,26,29]. During the synthesis of SiNWs, the etching solutions used for the metal-assisted chemical etching of Si can damage the sensor circuits; we use O-rings and a Teflon holder having a selective open area in the center on the rear of the sensor substrate. A Si substrate is cleaned by sequentially sonicating in acetone and methanol solutions. The substrate is cleaned further in the piranha solution for 40 min to remove organic materials. To synthesize the SiNWs, a cleaned Si surface of the substrate is coated with Ag^+ using a 5 mM $AgNO_3$ and 4.8 M HF solution for 1 min. $AgNO_3$ is ionized to Ag^+ and NO_3^- in aqueous solution, and

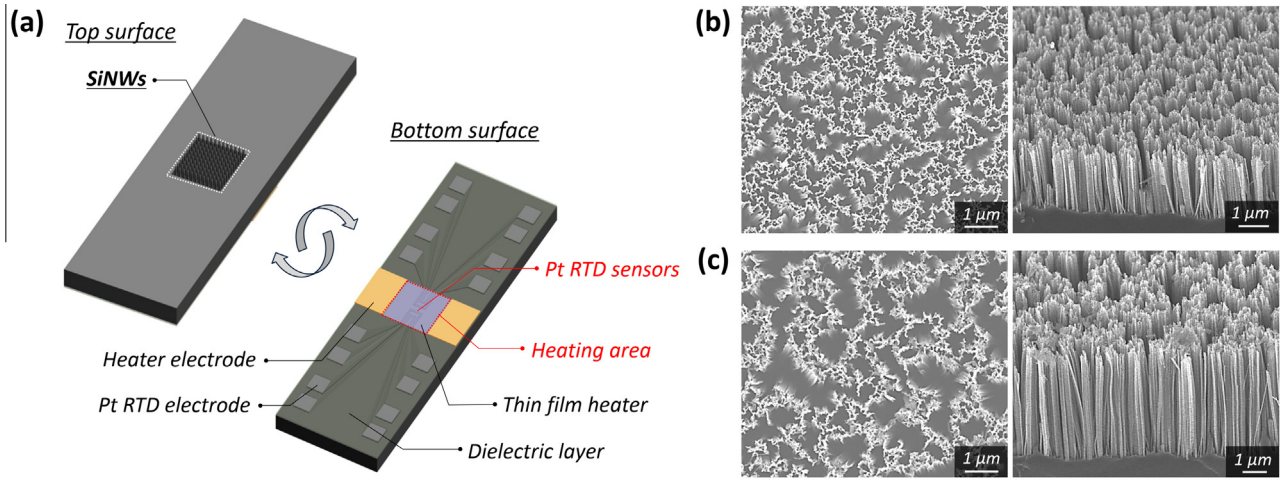

Fig. 1. Manipulated heat transfer surfaces: (a) schematics of the sensor chip with a film heater and RTD arrays. This figure is reprinted with permission from Elsevier [25]; (b) and (c) top and tilted views of FE-SEM images of vertically aligned SiNWs with an average height of 2.5 and 6.8 μm, respectively.

Ag^+ ions are reduced on the surface of the substrate. After rinsing the substrate with DI water, the sensor is dipped into a solution of 4.8 M HF and 0.1 M H_2O_2 for the synthesis of SiNWs. During the etching process, the Ag^+ ions act as a catalyst to generate holes through a cathode reaction (reduction of H_2O_2 to H_2O). The electric potential of Si is lower than that of Ag, thus the holes are transferred to the Si substrate. The local area under the reduced Ag is oxidized to SiO_2, and the HF solution selectively dissolves the SiO_2. As a result, the Si substrate is selectively etched away, and the remaining portions form vertically aligned SiNWs on the substrate [29]. The height of the nanowires is adjusted by controlling the etching time under ambient temperature and pressure conditions. Nanowires with heights of 2.5 μm and 6.8 μm are obtained by 10 min and 30 min etching, respectively, and they are presented in Fig. 1(b) and (c). Morphology and contact angle characterizations are conducted on manipulated surfaces with nanowires with heights of hundreds of nanometers to 15.8 μm.

2.3. Surface morphology characterization

Manipulated surface morphology is characterized by FE-SEM (JSM-7001F, JEOL, Japan) measurements. Through image processing, we determine the quantitative averages of the height of the SiNWs, distance between the SiNWs, and diameter of the SiNWs. The equivalent cavity sizes formed by the conglomerations of vertically aligned SiNWs are evaluated using I'MEASURE 2.0 software (ING PLUS, Korea). The SEM images of SiNWs with high contrast are used to determine the boundary of the naturally-formed microcavities. The imaging software automatically calibrates and then calculates equivalent cavity size along the boundary of the naturally-formed microcavities. More than 100 cavities with an area of 300 μm^2 were measured for each case of SiNWs.

2.4. Evaluation of static contact angle and hemi-wicking

We use a contact angle measuring system (KSV CAM-200, KSV Ins., Finland) to measure static CAs. Droplet images are collected with a high-speed camera using a frame interval of 2 ms and a resolution of 512 × 480 pixels and then static CAs are automatically analyzed by a calibrating program. The measurements are conducted using a 2.5 μL droplet of DI water and FC-72, and surrounding condition is controlled to the saturated-vapor pressure condition to exclude an evaporation effect near three-phase interface. The measurement is repeated at least five times, and static CAs are averaged from each case. To evaluate hemi-wicking the substrates with SiNWs are vertically immersed in DI water and FC-72. The hemi-wicking behavior is recorded using a high-speed camera (M310, Dantec, Denmark) at 100 fps, and the wicking distance is calibrated through post-imaging processing. The wicking distance is numerically determined by averaging results from at least three samples from each case. Movies showing hemi-wicking on the manipulated surface are included in the Supplementary Information.

3. Experimental

3.1. Closed-loop convective boiling system

The convective boiling system consists of a main circulating channel and a test section used for the installation of the sensor. Fig. 2 schematically presents the closed-loop experimental facilities and the test section used in this study [30–32]. A 3-kW immersion heater is inserted into a stainless steel reservoir with a capacity of 44 L to conduct preconditioning and to control the temperature of working fluids. A pressure gauge and K-type thermocouples are installed in the reservoir to monitor the conditions of the working fluid. A magnetic pump (TXS5.3, SUS316, Tuthill Co., USA) with an electric motor (LG-OTIS, Korea) is used to circulate the working fluid with a constant fluidic condition of the Reynolds number at Re = 12000 through a closed-loop channel containing a test section. Herein, the Reynolds number is used as a parameter to exclude property-dependent effects by the different fluids for comparative demonstrations about the presence of the morphologically-induced hemi-wicking. The closed-loop channel consists of stainless steel pipes wrapped with thermal insulation material to prevent heat loss. A mass-flow meter (Ultramass MK II, Oval Co., Japan) is installed in the channel to measure the flow rate. To accurately regulate the inlet temperature of the working fluid, we use a cross-flow heat exchanger connected to a constant temperature bath.

The test section is composed of an inlet settling chamber, a main channel which can be divided into an upper and a bottom part, and an outlet settling chamber made of polyether ether ketone (PEEK) with low thermal conductivity (Fig. 2(b)). The test section is thermally insulated during the experiments. The main channel has a length of 375 mm and a cross-sectional area of 5 × 5 mm^2. The main channel secures a flow-developing region of 200 mm before the heater, which is sufficient length to fully

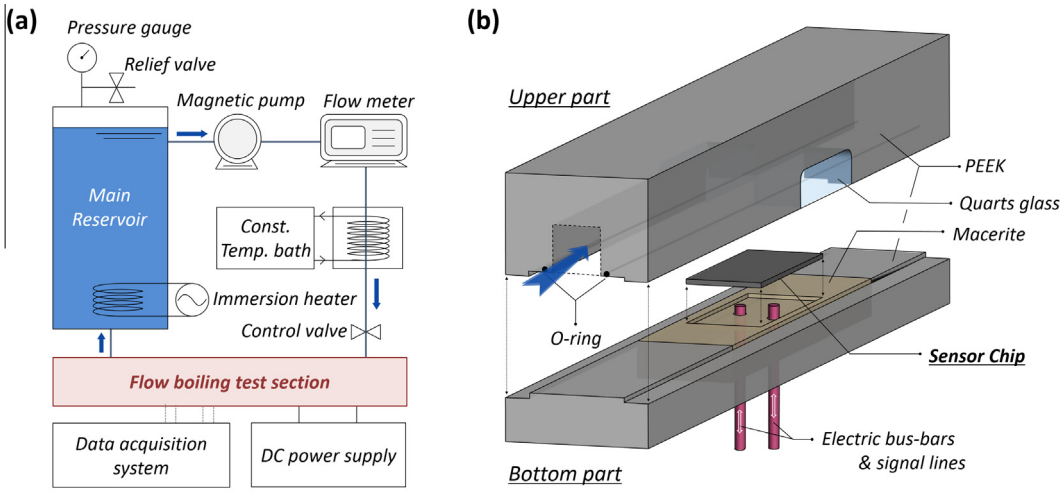

Fig. 2. Experimental facility for flow boiling characterization: (a) schematics of a closed-loop flow boiling system; (b) a test section for installing the fabricated sensor chip.

develop turbulent flow [33]. The fluid temperature is measured by J-type thermocouples (Omega, USA) in the inlet and outlet settling chamber. The sensor is aligned in the middle of the bottom part which is made of a ceramic Macerite for preventing conductive heat loss and thermal deformation during the experiments [25,26]. The sensor is firmly fixed onto the Macerite with a thin 0.1 mm-thick air gap layer between the sensor and the Macerite to prevent direct solid contact. Herein silicone gasket (Permatex, USA) is applied along the edge of the sensor in order to prevent liquid leakage. Two copper bus bars and spring probe wires are extruded passing through the Macerite for power delivery to ITO heater and electric signal detection from RTDs, respectively. After installation of the sensor on the bottom of the main channel, the two parts are assembled into a completed main channel. A DC power supply (200 V-10 A, KSC Korea Switching, Korea) is used to adjust the heat flux through the ITO film heater. Signals from the flow meter, thermocouples, and the heater in the sensor are acquired by a data logger (34970A, Agilent Technologies, USA) and processed using a desktop computer.

3.2. Data reduction and uncertainty analysis

3.2.1. Heat flux and critical heat flux

Applied heat flux is evaluated by estimating the applied current passing through the ITO film heater and the resultant voltage decrease. The heat flux is calculated by $q'' = Q_{actual}/A_{heater} = (V_{heater} \cdot I - Q_{loss})/A_{heater}$ where q'', Q, A, V, and I indicate the heat flux, heating power, heating area, voltage drop through the heater, and applied current, respectively. For the actual heat flux, we reflect the lateral conductive heat loss through the Si substrate. The loss is evaluated by 3D numerical analyses using a commercial code (ANSYS 15.0) and is compared with the experimental wall temperature data. When the heat flux approaches CHF, the local wall temperatures vigorously fluctuate. The heat flux generates bubbles that coalescence to form a thin vapor layer. The insulating vapor layer prevents heat from dissipating into the environment. In this study, we determine the heat flux at CHF by adding the heat flux measured at a temperature variation greater than 15 degrees centigrade and that half an increment from the previous step, just before increasing the heat flux [25,26,34].

3.2.2. Wall temperature

The temperatures from the RTDs are correlated to indicate the exact temperature of the back of the boiling surface, because the RTDs are on the opposite side of the Si substrate as the nanowires. Under the assumption that the Si substrate of the sensor is sufficiently thin (500 μm) for 1D heat conduction at a high thermal conductivity (~140 W m^{-1} K^{-1}), we derive the boiling surface temperatures of $T_w = T_{RTD} - (t_{Si}/k_{Si}) \cdot q''$ based on Fourier's 1D conduction law through the Si substrate [33,35]. Herein T_w, T_{RTD}, t_{Si}, and k_{Si} refer to the wall temperature on the boiling surface, temperature measured from RTDs, thickness of Si substrate, and thermal conductivity of the substrate, respectively.

3.2.3. Heat transfer coefficient

Convective heat dissipation ability or efficiency can be figured by the heat transfer coefficient, which indicates the boiling performance due to the temperature difference induced by buoyancy force, bubble nucleation/detachment from a heat dissipating surface and refreshing of liquid working fluid towards the surface. According to Newton's law of cooling, the convective heat transfer coefficient h can be expressed as $h = q''/(T_w - T_f)$ where T_f is the temperature of liquid working fluid, and controlled to the saturation temperature of the corresponding working fluid ($T_{sat,DI}$ = 100 °C and $T_{sat,FC\text{-}72}$ = 56 °C at atmospheric pressure). In this study, we use the Nusselt number ($Nu = h \cdot D_h/k_f$), a dimensionless factor for describing convective heat dissipation efficiency. Herein, D_h and k_f are the hydraulic diameter of the flow channel and thermal conductivity of the working fluid, respectively.

3.2.4. Uncertainty analysis

Uncertainty is estimated with a confidence level of 95%, accounting for fundamental dimensions and experimental variables [25,30,36]. The temperature measurement error using the employed thermocouple is 1.3 K, and the dimensional error of the fabricated sensor is 0.2%. The conductive heat loss through a silicon substrate, which has relatively high thermal conductivity, is analyzed by three-dimensional numerical analyses under a steady state condition using a commercial CFD code (ANSYS 15.0) to determine the uncertainty estimation of the applied heat flux [30]. The heat flux deviation due to spreading is considered conductive heat loss, and the evaluated heat loss uncertainty is 3.0%. Considering this heat loss uncertainty, we inversely predict the effective area at the top of the substrate which should dissipate the equivalent amount of an initial heat flux applied to the ITO heater. Based on the heat loss evaluation, the uncertainty of heat flux is calculated as $\delta q''/q'' = [(\delta V/V)^2 + (\delta I/I)^2 + (\delta A/A)^2 + (\delta q''_{loss}/q'')^2]^{1/2}$ where V, I, and A are the voltage decrease at the ITO heater, applied current, and area of the heater, respectively. The uncertainty is 3.5%. The wall temperature is evaluated based on Fourier's law describing one-dimensional conduction through the sensor substrate. Uncertainty of wall temperature can be expressed as $\delta T_w/T_w = [(\delta T_R/T_R)^2 + (\delta t_{Si}/t_{Si})^2 + (\delta k_{Si}/k_{Si})^2 + (\delta q''/q'')^2]^{1/2}$. The uncertainty of the wall temperature is 4.7%. The same procedure using related variables produces the uncertainty of the Nusselt number, which is 5.8%. Additionally, we compared the single-phase regime characteristics with an analytical prediction model suggested by Dittus and Boelter which is valid for single-phase heat transfer characteristics in turbulent regime [37].

4. Results and discussion

4.1. Morphology-induced hemi-wicking and roughness effects on boiling enhancement

When we consider boiling performance factors including CHF, HTC, and onset of nucleate boiling (ONB), the interfacial characteristics of the heat dissipating surface should be demonstrated regarding wettability and roughness, which are two principal factors determining the performance. Actual wettability is determined from surface free energy and surface morphology of the substrate [11]. As Wenzel and Cassie's model describe hydrophilic and hydrophobic states of wettability, respectively, roughness factor and solid fraction, which are alternative terms expressing the morphology, determine the affinity of the substrate for liquid fluids [38,39]. In particular, superhydrophilic states are determined using our previous approaches involving morphological wettability control and a prerequisite of dimensional criteria described as follows [11]:

$$h_{c,philic} \geqslant \frac{1}{\pi d}\left(\frac{1}{\cos\theta^*} - 1\right)(1-\varphi)(a+d)^2 \quad (2)$$

where $h_{c,philic}$, d and a represent the critical height of interfacial structures that can induce hemi-wicking to result in superhydrophilic characteristics, average diameter of SiNWs, and average distance between SiNWs, respectively. Fig. 3(a) shows that apparent CAs remarkably decrease with increasing surface roughness (for DI water through the increasing h of SiNWs from hundreds of nanometers to 15.8 μm). However, decoupled interfacial characteristics between the roughness and consequential static wetting can be

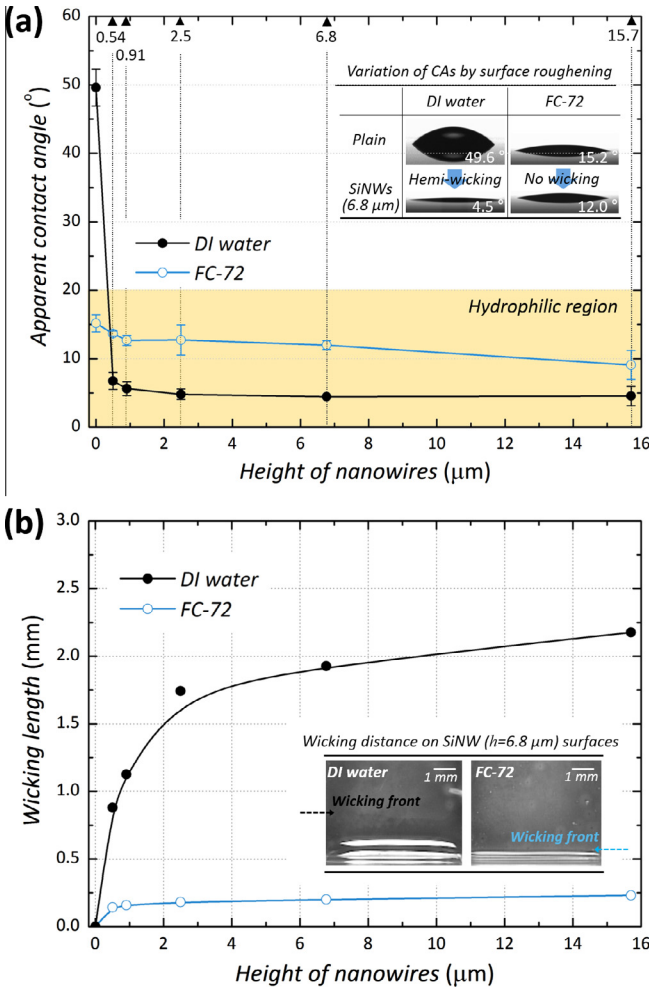

Fig. 3. Static wetting and morphologically-driven hemi-wicking characteristics: (a) apparent static contact angles on the manipulated surfaces of liquid drops of DI water and FC-72; (b) wicking propagation plots of the substrates immersed in the corresponding liquid.

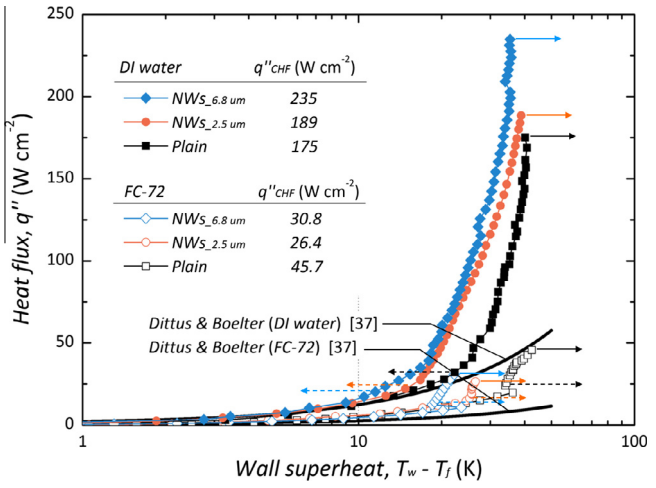

Fig. 4. Effects of the roughened interface w/ and w/o morphologically-driven hemi-wicking and convective boiling heat transfer performance. Horizontal arrows with solid lines and arrows with dotted lines indicate CHFs just before the abrupt temperature increase and onset of nucleation boiling (ONB), respectively.

realized using the highly-wettable refrigerant FC-72, which has a surface tension one order of magnitude lower than that of DI water. As confirmed from Fig. 3(a) and (b), the wettability of FC-72 does not have serious dependency on surface roughening within an intrinsic hydrophilic regime with a contact angle of 9–15°, while the roughening in DI water results in significant hemi-wicking and consequent superhydrophilic water-favoring behavior [11,26].

We are able to verify the effects of morphology-induced hemi-wicking on boiling performance by comparing the results on each manipulated surface with DI water accompanying hemi-wicking and FC-72 without wicking. Initially, CHF is demonstrated according to the interfacial effects. When the manipulated surface is accompanied by strong hemi-wicking with DI water, as shown in Fig. 4, CHF increases by 7.6% and 34% for 2.5 μm and 6.8 μm-heights of SiNWs, respectively, compared to that of the no-wicking surface (175.2 W cm^{-2}). The improvement in CHF is also found in recent previous studies based on micro/nanoscale interfacial structures causing dynamic wicking behavior with apparent superhydrophilicity [13,27,40]. However, the surface roughening in case of FC-72, which has relatively low surface tension, results in a rather detrimental variation in CHF. This difference can be explained regarding the presence of hemi-wicking caused by interfacial capillary effects, which is essential for refreshing liquids on the surface and for extending CHF [26]. The morphology-induced hemi-wicking is effective to refresh liquid coolant toward the interface, and the refreshing retards CHF by maintaining stability and balancing between up-ward moving bubbles and counteracting liquid on the surface. Even though SiNWs are used on the heat dissipating surface with extreme roughness, they do not have a remarkable driving effect on the wicking in the presence of a highly wetting liquid such as a FC-72 refrigerant. This is consistent with previous studies on roughness, where enhancement of CHF was not guaranteed without improving surface affinity with a working fluid [41]. Without any associated benefits such as interfacial hydrodynamics, SiNWs just causes a mere surface roughening. As the roughening must be a necessary condition but not a sufficient condition especially for CHF extension [41–43], the mere surface roughening rather offers obstacles such as: prevention of ebullition of vaporized bubbles on the roughened surface by entangled nanostructures [42]; deterioration of liquid accessibility towards the heat dissipation surface by increasing viscous resistance. In particular, the roughened structures of intricately arranged SiNWs just inhibit the escape of nucleated bubbles. Surface roughness is not a major factor for improving CHF, but it could be manipulated to obtain favorable hydrodynamic refreshing by interfacial capillary pumping [26,42,43].

4.2. Morphological roughening for initiating nucleation and convective heat dissipation

Enhanced convective heat dissipation efficiency can be expected for both working fluids with and without hemi-wicking through the process of surface roughening. Fig. 4 shows that the surface roughening leads to a decrease in wall superheat with both working fluids. In particular, we indicate a dimensionless factor of the Nusselt number ($Nu = h \cdot D_h/k_f$) in Fig. 5 describing convective heat dissipation efficiency. Even though the two working fluids show somewhat different distributions of heat dissipating performance owing to the significant disparity in their intrinsic properties such as the latent heat of vaporization, l (an indicator for onset of phase change; l_{DI} = 2270 kJ kg^{-1} and $l_{FC\text{-}72}$ = 88 kJ kg^{-1}) and thermal conductivity, k (k_{DI} = 0.6 W m^{-1} K^{-1} and $k_{FC\text{-}72}$ = 0.057 W m^{-1} K^{-1}), higher SiNWs result in improvement in convective efficiency for heat dissipation. As the height of the SiNWs increases, the roughness factor increases, reinforcing the static hydrophilicity [11]. Without accounting for the subsidiary

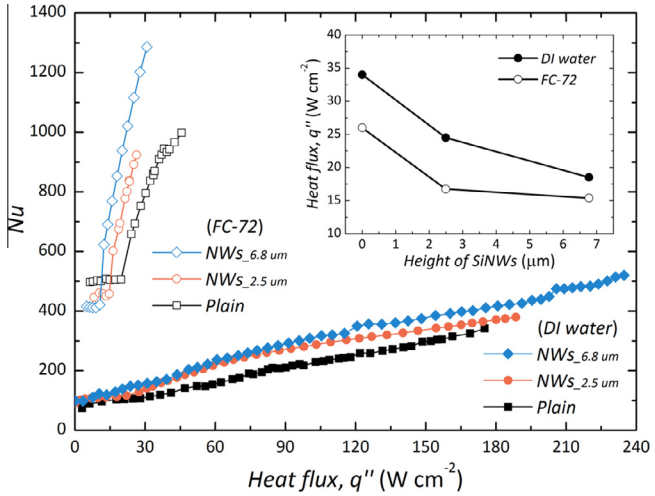

Fig. 5. Effects of surface roughening using SiNWs during convective heat dissipation of each working fluid. The Nusselt number ($Nu = hD_h/k_f$) represents the dimensionless performance factor indicating convection at the interface. The inset presents the heat flux at the onset of nucleation accompanying the phase change of the working fluid.

effect of hemi-wicking, we find that surface roughening effectively promotes convective heat dissipation. The enlarged interfacial area between the working fluid and heat-dissipating surface contributes to convective heat dissipation. In addition, the static surface wettability is closely related to nucleation under boiling environments. Based on the static wettability characteristics, the effective cavity range can be theoretically explained based on the development of the thermal boundary layer supplying nucleation-initiating thermal energy, as follows [44–47]:

$$\{r_{c,min}, r_{c,max}\} = \frac{\delta_t \sin\theta_b}{2.2}\left(\frac{\Delta T_{sat}}{\Delta T_{sat}+\Delta T_{sub}}\right) \times \left[1 \mp \sqrt{1-\frac{9.2\sigma T_{sat}(\Delta T_{sat}+\Delta T_{sub})}{\rho_v l_{LV}\delta_t \Delta T_{sat}^2}}\right] \quad (3)$$

where δ_t, θ_b, σ, ΔT_{sat}, ΔT_{sub}, ρ_v, and l_{LV} are the thermal boundary layer thickness, contact angle between bubble and wall, surface tension of fluid, wall superheat, liquid subcooling, vapor density, and latent heat, respectively. Herein, θ_b is defined by averaging an upstream and a downstream contact angle of a nucleated bubble under flow boiling environments [45]. Actual bubbles would be readily detachable in superhydrophilic condition created by SiNWs (i.e., morphological roughening) and low surface tension of liquid (i.e., FC-72), and consequentially the nucleated bubbles could maintain a sphere-shape less biased against flow momentum because of the enhanced liquid penetration and their own size diminution with more fast ebullition frequency [48]. Thus we assume that θ_b converges to static contact angle, which is intermediate value between upstream and downstream contact angle according to the hydrodynamic limit around bubble [45]. Fig. 6(a) shows the expected range of effective cavity size based on the working fluids used. For DI water, the effective cavity size at the onset is up to 9 μm and decreases to 1–2 μm when SiNWs with a height of 6.8 μm induce superhydrophilicity with an apparent CA of 4.5°. The roughening and consequent hydrophilicity also make the effective cavities with the refrigerant smaller as they do with DI water. Actual cavity structures that correspond to these prerequisites in size practically support and catalyze nucleation. Vertically aligned long SiNWs are confirmed to accompany micron-scale by-productive cavities formed by longitudinal coalescence due to van der Waals forces [25,49,50]. In this study, we verify the results shown in Fig. 6(b)

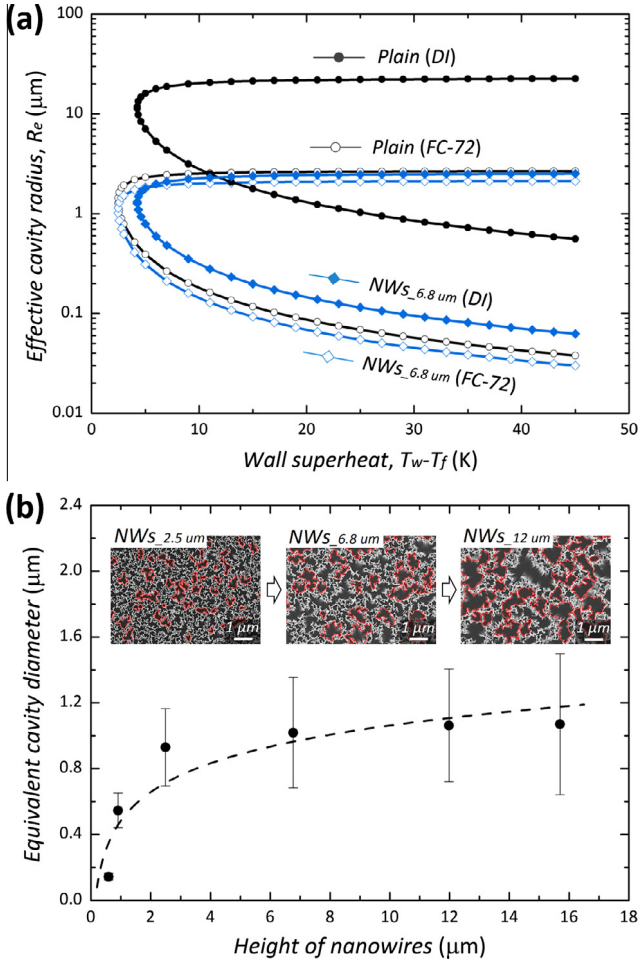

Fig. 6. Effective cavity size for nucleate boiling, and actual cavities formed by SiNWs: (a) analytical estimation of effective cavity sizes on plain and SiNWs-modified ($l = 6.8$ μm) surfaces for each working fluid; (b) equivalent cavity sizes (averaged values with standard deviations) formed by the conglomeration of long SiNWs. The black dashed line presents a curve fitting of approximation of the equivalent cavity sizes.

within the domain of SiNWs' height below 16 μm. This guarantees that the effective cavity sizes in a certain boiling environment (Fig. 6(a)) are well matched to the natural cavity sizes on the surface manipulated via SiNWs. The natural nucleation sites facilitate discrete bubble formations. The ONB presented in the inset of Fig. 5 is explained by surface roughening and the actual cavities. The roughening promotes nucleation by decreasing the required heat flux at ONB. As we increase the height of the SiNWs and create a greater number of larger cavities that fulfill the prerequisite for effective cavity range, nucleation becomes more efficient and results in lower wall superheats. For both fluids, with and without regard to the variations in intrinsic surface tension, the morphological aspects of nucleation contribute to initiation of nucleation and higher convective heat dissipation efficiency.

5. Conclusion

Superhydrophilicity accompanying hemi-wicking driven by interfacial capillary force can be realized by constructing interfacial structures. Morphologically driven hemi-wicking on a roughened interface is essential to promoting a principal boiling performance factor of the allowable convective heat dissipation capacity of CHF. The roughened morphology with cavity-like structures is favorable to enhancing the convective heat dissipation efficiency of HTC for

more efficient thermal energy dissipation. We presented that the roughened surface without the creation of the hemi-wicking, which should be required for interfacial liquid refreshing and must be dependent on properties of a working fluid, rather deteriorates CHF performance. For feasible creation of hemi-wicking, we applied a design prerequisite [10,11], which have confined the presence of the interfacial wicking, and presented the characterization of wicking by controlling characteristic lengths of nanoscale structures and consequent enhancements of the boiling performance. Interfacial liquid refreshing through the morphologically driven hemi-wicking led to a greater than 100% increase in CHF and was realized by roughening surfaces using vertically aligned SiNWs. Dimensional prerequisites initiating hemi-wicking with regard to the characteristic length of SiNWs can be a potential design guideline for practical engineering applications with its feasibility and reliability.

Acknowledgments

This work was supported by the Human Resources Development Program (No. 20144030200560) of the Korea Institute of Energy Technology Evaluation and Planning (KETEP) funded by the Korean government Ministry of Trade, Industry and Energy. B.S.K acknowledges the Alexander von Humboldt foundation (AvH) for support through a Humboldt Research Fellowship (3.5-KOR/1159778 STP).

Appendix A. Supplementary data

Supplementary data associated with this article can be found, in the online version, at http://dx.doi.org/10.1016/j.ijheatmasstransfer.2016.07.008.

References

[1] J.G. Fan, D. Dyer, G. Zhang, Y.P. Zhao, Nanocarpet effect: pattern formation during the wetting of vertically aligned nanorod arrays, Nano Lett. 4 (2004) 2133–2138, http://dx.doi.org/10.1021/nl048776b.
[2] E. Martines, K. Seunarine, H. Morgan, N. Gadegaard, C.D.W. Wilkinson, M.O. Riehle, Superhydrophobicity and superhydrophilicity of regular nanopatterns, Nano Lett. 5 (2005) 2097–2103, http://dx.doi.org/10.1021/nl051435t.
[3] F.C. Cebeci, Z.Z. Wu, L. Zhai, R.E. Cohen, M.F. Rubner, Nanoporosity-driven superhydrophilicity: a means to create multifunctional antifogging coatings, Langmuir 22 (2006) 2856–2862, http://dx.doi.org/10.1021/la053182p.
[4] S.P.R. Kobaku, A.K. Kota, D.H. Lee, J.M. Mabry, A. Tuteja, Patterned superomniphobic–superomniphilic surfaces: templates for site-selective self-assembly, Angew. Chem.-Int. Edit. 51 (2012) 10109–10113, http://dx.doi.org/10.1002/anie.201202823.
[5] Y. Coffinier, G. Piret, M.R. Das, R. Boukherroub, Effect of surface roughness and chemical composition on the wetting properties of silicon-based substrates, C. R. Chim. 16 (2013) 65–72, http://dx.doi.org/10.1016/j.crci.2012.08.011.
[6] J. Bico, C. Tordeux, D. Quéré, Rough wetting, Europhys. Lett. 55 (2001) 214–220, http://dx.doi.org/10.1209/epl/i2001-00402-x.
[7] C.W. Extrand, S.I. Moon, P. Hall, D. Schmidt, Superwetting of structured surfaces, Langmuir 23 (2007) 8882–8890, http://dx.doi.org/10.1021/la700816n.
[8] C. Ishino, M. Reyssat, E. Reyssat, K. Okumura, D. Quéré, Wicking within forests of micropillars, Europhys. Lett. 79 (2007) 56005, http://dx.doi.org/10.1209/0295-5075/79/56005.
[9] J. Drelich, E. Chibowski, Superhydrophilic and superwetting surfaces: definition and mechanisms of control, Langmuir 26 (2010) 18621–18623, http://dx.doi.org/10.1021/la1039893.
[10] J. Bico, U. Thiele, D. Quéré, Wetting of textured surfaces, Colloid Surf. A-Physicochem. Eng. Asp. 206 (2002) 41–46, http://dx.doi.org/10.1016/S0927-7757(02)00061-4.
[11] B.S. Kim, S. Shin, S.J. Shin, K.M. Kim, H.H. Cho, Control of superhydrophilicity/superhydrophobicity using silicon nanowires via electroless etching method and fluorine carbon coatings, Langmuir 27 (2011) 10148–10156, http://dx.doi.org/10.1021/la200940j.
[12] V.S. Nikolayev, D. Chatain, Y. Garrabos, D. Beysens, Experimental evidence of the vapor recoil mechanism in the boiling crisis, Phys. Rev. Lett. 97 (2006) 184503, http://dx.doi.org/10.1103/PhysRevLett. 97.184503.
[13] R. Chen, M.C. Lu, V. Srinivasan, Z. Wang, H.H. Cho, A. Majumdar, Nanowires for enhanced boiling heat transfer, Nano Lett. 9 (2009) 548–553, http://dx.doi.org/10.1021/nl8026857.
[14] C.C. Hsu, P.H. Chen, Surface wettability effects on critical heat flux of boiling heat transfer using nanoparticle coatings, Int. J. Heat Mass Transfer 55 (2012) 3713–3719, http://dx.doi.org/10.1016/j.ijheatmasstransfer.2012.03.003.
[15] Z. Wu, B. Sundén, On further enhancement of single-phase and flow boiling heat transfer in micro/minichannels, Renew. Sust. Energy Rev. 40 (2014) 11–27, http://dx.doi.org/10.1016/j.rser.2014.07.171.
[16] J. Kim, Review of nucleate pool boiling bubble heat transfer mechanisms, Int. J. Multiph. Flow 35 (2009) 1067–1076, http://dx.doi.org/10.1016/j.ijmultiphaseflow.2009.07.008.
[17] B. Feng, K. Weaver, G.P. Peterson, Enhancement of critical heat flux in pool boiling using atomic layer deposition of alumina, Appl. Phys. Lett. 100 (2012) 053120, http://dx.doi.org/10.1063/1.3681943.
[18] J.S. Coursey, J. Kim, Nanofluid boiling: the effect of surface wettability, Int. J. Heat Fluid Flow 29 (2008) 1577–1585, http://dx.doi.org/10.1016/j.ijheatfluidflow.2008.07.004.
[19] I.L. Pioro, W. Rohsenow, S.S. Doerffer, Nucleate pool-boiling heat transfer. I: Review of parametric effects of boiling surface, Int. J. Heat Mass Transfer 47 (2004) 5033–5044, http://dx.doi.org/10.1016/j.ijheatmasstransfer.2004.06.019.
[20] K. Chu, R. Enright, E.N. Wang, Structured surfaces for enhanced pool boiling heat transfer, Appl. Phys. Lett. 100 (2012) 241603, http://dx.doi.org/10.1063/1.4724190.
[21] H. Hanley, C. Coyle, J. Buongiorno, T. McKrell, L. Hu, M. Rubner, R. Cohen, Separate effects of surface roughness, wettability, and porosity on the boiling critical heat flux, Appl. Phys. Lett. 103 (2013) 024102, http://dx.doi.org/10.1063/1.4813450.
[22] C. Li, Z. Wang, P.I. Wang, Y. Peles, N. Koratkar, G.P. Peterson, Nanostructured copper interfaces for enhanced boiling, Small 4 (2008) 1084–1088, http://dx.doi.org/10.1002/smll.200700991.
[23] N.A. Patankar, Supernucleating surfaces for nucleate boiling and dropwise condensation heat transfer, Soft Matter 6 (2010) 1613–1620, http://dx.doi.org/10.1039/b923967g.
[24] B. Bourdon, R. Rioboo, M. Marengo, E. Gosselin, J. De Coninck, Influence of the wettability on the boiling onset, Langmuir 28 (2012) 1618–1624, http://dx.doi.org/10.1021/la203636a.
[25] B.S. Kim, S. Shin, D. Lee, G. Choi, H. Lee, K.M. Kim, H.H. Cho, Stable and uniform heat dissipation by nucleate-catalytic nanowires for boiling heat transfer, Int. J. Heat Mass Transfer 70 (2014) 23–32, http://dx.doi.org/10.1016/j.ijheatmasstransfer.2013.10.061.
[26] B.S. Kim, H. Lee, S. Shin, G. Choi, H.H. Cho, Interfacial wicking dynamics and its impact on critical heat flux of boiling heat transfer, Appl. Phys. Lett. 105 (2014) 191601, http://dx.doi.org/10.1063/1.4901569.
[27] D. Li, G.S. Wu, W. Wang, Y.D. Wang, D. Liu, D.C. Zhang, Y.F. Chen, G.P. Peterson, R. Yang, Enhancing flow boiling heat transfer in microchannels for thermal management with monolithically-integrated silicon nanowires, Nano Lett. 12 (2012) 3385–3390, http://dx.doi.org/10.1021/nl300049f.
[28] S. Kim, D. Khang, Bulk micromachining of Si by metal-assisted chemical etching, Small 10 (2014) 3761–3766, http://dx.doi.org/10.1002/smll.201303379.
[29] Z. Huang, N. Geyer, P. Werner, J. de Boor, U. Gösele, Metal-assisted chemical etching of silicon: a review, Adv. Mater. 23 (2011) 285–308, http://dx.doi.org/10.1002/adma.201001784.
[30] G. Choi, B.S. Kim, H. Lee, S. Shin, H.H. Cho, Jet impingement in a crossflow configuration: convective boiling and local heat transfer characteristics, Int. J. Heat Fluid Flow 50 (2014) 378–385, http://dx.doi.org/10.1016/j.ijheatfluidflow.2014.09.010.
[31] S. Shin, G. Choi, B.S. Kim, H.H. Cho, Flow boiling heat transfer on nanowire-coated surfaces with highly wetting liquid, Energy 76 (2014) 428–435, http://dx.doi.org/10.1016/j.energy.2014.08.037.
[32] B.S. Kim, G.M. Yang, S. Shin, G. Choi, H.H. Cho, Local nucleation propagation on heat transfer uniformity during subcooled convective boiling, Heat Mass Transfer 51 (2015) 1–9, http://dx.doi.org/10.1007/s00231-014-1379-0.
[33] F.P. Incropera, Fundamentals of Heat and Mass Transfer, sixth ed., John Wiley, Hoboken, N.J., 2007.
[34] K.N. Rainey, S.M. You, Effects of heater size and orientation on pool boiling heat transfer from microporous coated surfaces, Int. J. Heat Mass Transfer 44 (2001) 2589–2599, http://dx.doi.org/10.1016/s0017-9310(00)00318-5.
[35] A.F. Mills, Basic Heat and Mass Transfer, second ed., Prentice Hall, Upper Saddle River, N.J., 1999.
[36] S.J. Kline, The purposes of uncertainty analysis, J. Fluids Eng. 107 (1985) 153–160, http://dx.doi.org/10.1115/1.3242449.
[37] F.W. Dittus, L.M.K. Boelter, Heat transfer in automobile radiators of the tubular type, Int. Commun. Heat Mass Transfer 12 (1985) 3–22, http://dx.doi.org/10.1016/0735-1933(85)90003-X.
[38] R.N. Wenzel, Resistance of solid surfaces to wetting by water, Ind. Eng. Chem. 28 (1936) 988–994, http://dx.doi.org/10.1021/ie50320a024.
[39] A.B.D. Cassie, S. Baxter, Wettability of the porous surfaces, Trans. Faraday Soc. 40 (1944) 546–551, http://dx.doi.org/10.1039/TF9444000546.
[40] M.C. Lu, R.K. Chen, V. Srinivasan, V. Carey, A. Majumdar, Critical heat flux of pool boiling on Si nanowire array-coated surfaces, Int. J. Heat Mass Transfer 54 (2011) 5359–5367, http://dx.doi.org/10.1016/j.ijheatmasstransfer.2011.08.007.
[41] B. Stutz, C.H.S. Morceli, M.D. da Silva, S. Cioulachtjian, J. Bonjour, Influence of nanoparticle surface coating on pool boiling, Exp. Therm. Fluid Sci. 35 (2011) 1239–1249, http://dx.doi.org/10.1016/j.expthermflusci.2011.04.011.

[42] V. Khanikar, I. Mudawar, T. Fisher, Effects of carbon nanotube coating on flow boiling in a micro-channel, Int. J. Heat Mass Transfer 52 (2009) 3805–3817, http://dx.doi.org/10.1016/j.ijheatmasstransfer.2009.02.007.
[43] K. Chu, Y.S. Joung, R. Enright, C.R. Buie, E.N. Wang, Hierarchically structured surfaces for boiling critical heat flux enhancement, Appl. Phys. Lett. 102 (2013) 151602, http://dx.doi.org/10.1063/1.4801811.
[44] Y.Y. Hsu, On the size range of active nucleation cavities on a heating surface, J. Heat Transf.-Trans. ASME 84 (1962) 207–213, http://dx.doi.org/10.1115/1.3684339.
[45] S.G. Kandlikar, B.J. Stumm, A control volume approach for investigating forces on a departing bubble under subcooled flow boiling, J. Heat Transf.-Trans. ASME 117 (1995) 990–997, http://dx.doi.org/10.1115/1.2836321.
[46] S.G. Kandlikar, V. Mizo, M. Cartwright, E. Ikenze, Bubble nucleation and growth characteristics in subcooled flow boiling of water, in: ASME Proceedings of the 32nd National Heat Transfer Conference, 4, 1997, pp. 11–18.
[47] S.G. Kandlikar, Heat transfer characteristics in partial boiling, fully developed boiling, and significant void flow regions of subcooled flow boiling, J. Heat Transf.-Trans. ASME 120 (1998) 395–401, http://dx.doi.org/10.1115/1.2824263.
[48] A.R. Betz, J. Xu, H.H. Qiu, D. Attinger, Do surfaces with mixed hydrophilic and hydrophobic areas enhance pool boiling?, Appl Phys. Lett. 97 (2010) 141909, http://dx.doi.org/10.1063/1.3485057.
[49] Y.A. Dai, H.C. Chang, K.Y. Lai, C.A. Lin, R.J. Chung, G.R. Lin, J.H. He, Subwavelength Si nanowire arrays for self-cleaning antireflection coatings, J. Mater. Chem. 20 (2010) 10924–10930, http://dx.doi.org/10.1039/c0jm00524j.
[50] T.T. Mai, C.Q. Lai, H. Zheng, K. Balasubramanian, K.C. Leong, P.S. Lee, C. Lee, W. K. Choi, Dynamics of wicking in silicon nanopillars fabricated with interference lithography and metal-assisted chemical etching, Langmuir 28 (2012) 11465–11471, http://dx.doi.org/10.1021/la302262g.